

AN EULEREAN FINITE ELEMENT MODEL FOR PENETRATION IN LAYERED SOIL

PETER VAN DEN BERG

Delft Geotechnics, P.O. Box 69, 2600 AB Delft, the Netherlands

RENÉ DE BORST

Delft University of Technology and Eindhoven University of Technology, the Netherlands

AND

HAN HUÉTINK

University of Twente, the Netherlands

SUMMARY

An Eulerian large-strain finite element formulation is presented to simulate static soil penetration. The method is an extension of the Updated Lagrangean description to an Eulerian formulation taking into account convection of deformation-history-dependent properties as well as material properties. The strength of the soil is characterized by a non-associated Drucker–Prager criterion which depends on peak and critical friction angles. The model is applied to cone penetration in two-layer systems: (a) clay on sand and (b) sand on clay.

KEY WORDS: finite element method; large deformation; cone penetration test; layered soil

1. INTRODUCTION

Many important *in situ* soil tests involve large plastic deformations, e.g. the cone penetration test, the continuous sampling test and the vane test. Often, it is desirable to have a relation between the real soil properties, like Young's modulus, cohesion and friction angle and the forces and other data that are measured during such an *in situ* test. Since the geometry of these problems is often quite complex, analytical tools can normally only be used in an approximate manner. Nevertheless, many approaches that are most useful in geotechnical practice have been developed in this fashion. We mention the cavity expansion theory¹ and the strain path method² as clear examples in the case of the cone penetration test.

In principle, numerical techniques, in particular the finite element method allow for a rigorous solution of the above boundary value problems, without making concessions when modelling geometry or material behaviour. Yet, computational procedures are often not yet so far developed, that a solution can be provided that is directly useful in geotechnical practice. For the case of a cone penetration test for instance, a reliable solution that properly takes into account the large plastic deformations, is still not available. Indeed, it is only some fifteen years ago that the first small-strain finite element analyses started to emerge.^{3, 4} Essentially, a penetrometer was inserted in a pre-bored hole and a small-strain analysis was carried out for an undisturbed soil mass. To erase the incorrect assumption of a pre-bored hole as initial condition, a large-strain finite element formulation is needed,^{5–7} and with it the problem came that use of a conventional

Updated Lagrange method quickly results in highly distorted elements, yielding highly inaccurate answers or even divergence of the computational procedure.

In this contribution an Eulerean framework is used, thus preventing any unwanted element distortion. In fact, the adopted Eulerean framework is a special case of the so-called Arbitrary Lagrangean Eulerean (ALE) method, in which the movement of the element nodes and the material points is decoupled. This provides a general framework for mesh adaptivity. Here we select the special case of fixed element nodes.

Arbitrary Lagrangean Eulerean methods are not new and have been developed initially for fluid mechanics applications^{8,9} and have later been used to describe metal forming processes.^{10–12} The novel aspects of the present contribution are its application to a typical, albeit rather crude, soil model, and the extension of the method to layered systems, which is a case normally encountered in geotechnical engineering, e.g. sand–clay layered deposits.

This paper is organized as follows. Firstly, some aspects concerning large deformations are recapitulated and the governing finite element equations for large deformations are briefly outlined. Then, the algorithm for transfer of the stresses and the state variables is discussed in some detail. Next, the extension is made to layered systems, and an example involving elasticity is presented to demonstrate the correctness of the algorithm. After a succinct discussion of the adopted elasto-plastic constitutive model, an analysis is presented of the cone penetration test. Firstly, a homogeneous soil deposit is considered, and issues like convergence of the solution upon mesh refinement are addressed. Then, two cases of layered soil deposits are analysed, one case of clay on sand, and one case of sand on clay.

It is emphasized that the main thrust of this article is the development of a general numerical methodology for analysing *in situ* soil tests in layered deposits, and that quantitative assessment of a specific test is beyond the scope of this article. Indeed, this also holds true for the analysed case of a cone penetration test, although the qualitative results can already be insightful.

2. FINITE ELEMENT FORMULATION

Two different approaches can be chosen to describe the kinematics of a continuous body undergoing finite deformations: a Lagrangean formulation in which stresses and strains are defined with respect to a fixed co-ordinate system and an Eulerean formulation based on a convected co-ordinate system. The Eulerean approach will be followed in the present study, although the same set of resulting equations can be obtained using the Green–Lagrange strain and the 2nd Piola–Kirchhoff stress.¹² For an Eulerean description, it is most common to characterize the deformation process using the velocity gradient v_{ij} . The notation j implies differentiation with respect to x_j , the j -co-ordinate of the spatial (or Eulerean) co-ordinates and a superimposed dot denotes differentiation with respect to time. The velocity gradient is defined as

$$v_{i,j} = \dot{F}_{ik} F_{jk}^{-1} \quad (1)$$

where F_{ij} is the deformation gradient, and can be decomposed into a symmetric part (rate of deformation or rate of stretching) and a skew-symmetric part (the spin or vorticity tensor):

$$v_{i,j} = d_{ij} + \omega_{ij} \quad (2)$$

with

$$d_{ij} = \frac{1}{2}(v_{i,j} + v_{j,i}) \quad (3)$$

$$\omega_{ij} = \frac{1}{2}(v_{i,j} - v_{j,i}) \quad (4)$$

Starting from a thermo-dynamical point of view, the stress state in a material is a function of deformation, density, time and temperature.¹³ When thermal and time-dependent effects are not taken into account, the stress state in a material only depends on the deformation and the density of the material. Therefore, the constitutive equation for an elastoplastic material can be written in the following general rate-type formulation:

$$\dot{\sigma}_{ij}^o = \frac{\dot{\rho}}{\rho} \sigma_{ij} + D_{ijkl} d_{kl} \quad (5)$$

in which D_{ijkl} is a fourth-order tensor depending on material parameters. The term with ρ (mass density) results from the natural reference theory.¹³

In finite deformation analyses an objective stress rate, $\dot{\sigma}_{ij}^o$, is needed in the definition of the constitutive model. A widely used stress rate satisfying objectivity is the Jaumann stress rate:

$$\dot{\sigma}_{ij}^o = \dot{\sigma}_{ij} + \sigma_{ik} \omega_{kj} - \omega_{ik} \sigma_{kj} \quad (6)$$

Although a large number of objective stress rate definitions exist,¹⁴⁻¹⁶ it is important to recognize that, whichever formulation is adopted, identical results are obtained if the constitutive law for each description is developed correctly, if proper consideration is given with respect to the finite rotation effects during the numerical integration of constitutive equations and if the virtual-work principle is used correctly to set up the finite element equations.¹⁷

Combining equations (5) and (6) yields the Cauchy stress rate $\dot{\sigma}_{ij}$.

$$\dot{\sigma}_{ij} = D_{ijkl} d_{kl} - \sigma_{ik} \omega_{kj} + \omega_{ik} \sigma_{kj} - \sigma_{ij} d_{kk} \quad (7)$$

in which $d_{kk} = -\dot{\rho}/\rho$.

In a weak format the equilibrium condition can be expressed as

$$\delta W = \int_V \sigma_{ij} \delta d_{ij} dV - \int_V \rho F_i \delta v_i dV - \int_S T_i \delta v_i dS = 0 \quad (8)$$

with V the current volume of the material, the δ -symbol denoting virtual quantities, F_i the force per unit mass, S the current boundary surface and T_i the surface force per unit area.

In order to obtain an expression in which the relation between stress rate and deformation rate can be substituted the material time derivative of the virtual power (equation (8)) has to be taken. In a large deformation analysis the integration area is not constant, so the material rate of change of an integral with changing integration area has to be considered, and we obtain

$$\begin{aligned} (\delta \dot{W}) = & \int_V [\dot{\sigma}_{ij} \delta d_{ij} + \sigma_{ij} \delta \dot{d}_{ij} d_{kk}] dV \\ & - \int_V [(\rho \dot{F}_i) \delta v_i + \rho F_i \delta \dot{v}_i d_{kk}] dV \\ & - \int_S [\dot{T}_i \delta v_i + T_i \delta \dot{v}_i v_{\alpha, \alpha}] dS = 0 \end{aligned} \quad (9)$$

since the terms containing the time derivative of the virtual rate of deformation and the time derivative of the virtual velocity vanish. The indices α denote that the surface components of the

velocity are considered. Introducing equation (7) into equation (9) results in

$$\begin{aligned}
 (\delta \dot{W}) = & \int_V [\delta d_{ij} (D_{ijkl} d_{kl} - \sigma_{ik} \omega_{kj} + \omega_{ik} \sigma_{kj} - \sigma_{ij} d_{kk}) + \sigma_{ij} \delta d_{ij} d_{kk}] dV \\
 & - \int_V [(\rho \dot{F}_i) \delta v_i + \rho F_i \delta v_i d_{kk}] dV \\
 & - \int_S [\dot{T}_i \delta v_i + T_i \delta v_i v_{\alpha, \alpha}] dS = 0
 \end{aligned} \quad (10)$$

Using equations (2)–(4) and the relation

$$(\rho \dot{F}_i) = \rho \dot{F}_i - \rho F_i d_{kk} \quad (11)$$

yields

$$\begin{aligned}
 (\delta \dot{W}) = & \int_V [D_{ijkl} d_{kl} \delta d_{ij} - 2\sigma_{kj} d_{ik} \delta d_{ij} + \sigma_{ij} v_{k,j} \delta v_{k,i}] dV \\
 & - \int_V [\rho \dot{F}_i \delta v_i] dV - \int_S [T_i \delta v_i + T_i \delta v_i v_{\alpha, \alpha}] dS = 0
 \end{aligned} \quad (12)$$

The finite element method is applied to solve the set of resulting equations. Then equation (12) can be written in the following discretized form (in matrix notation):

$$(\delta \dot{W}) = \delta v^T \mathbf{S} v - \delta v^T \dot{k} \quad (13)$$

where

$$\begin{aligned}
 \mathbf{S} = & \int_V [\mathbf{B}^T (\mathbf{D} - \boldsymbol{\Sigma}_1) \mathbf{B}] dV + \int_V [(\mathbf{L}\psi)^T \boldsymbol{\Sigma}_2 (\mathbf{L}\psi)] dV \\
 & - \int_S [\psi^T \mathbf{T} (\mathbf{L}\psi)] dS
 \end{aligned} \quad (14)$$

and

$$k = \int_V (\psi^T \rho \dot{F}) dV + \int_S (\psi^T \dot{T}) dS \quad (15)$$

Here \mathbf{B} is the discrete strain operator, \mathbf{L} is a matrix containing differential operators, ψ is an interpolation function and the matrices $\boldsymbol{\Sigma}_1$ and $\boldsymbol{\Sigma}_2$ contain Cauchy stress components.¹⁸ Requiring that equation (13) is equal to zero for arbitrary values of the virtual nodal velocities yields the following set of equations:

$$\mathbf{S} \cdot v = k \quad (16)$$

The stiffness matrix \mathbf{S} may be non-symmetric, because of non-symmetry of \mathbf{D} , which arises if a non-associated flow-rule is employed, and because of the last term in equation (14), which only appears in the presence of surface forces.

If at time t the shape, state of stress and boundary conditions are known, the nodal point velocities can be solved. Within a time increment Δt the material displacement increments of the nodal points are approximated by

$$\Delta u_i^N = v_i^N \cdot \Delta t \quad (17)$$

So far the method is identical to the Updated Lagrangean approach,^{18,19} where the nodal points are coupled with the material points. The Updated Lagrangean method has the notable disadvantage that, if large local deformations occur, elements can be highly distorted or even turned inside out. This problem can be avoided using adaptive meshing or remeshing. Here, we will use an *r*-adaptivity technique, the so-called Arbitrary Lagrangean–Eulerean formulation (ALE), in which nodal point displacements and velocities and material displacements and velocities are decoupled. This implies that the material can flow through the elements. The so-called operator split algorithm is used in which, first, implicitly a Lagrangean step is calculated and, subsequently, convection is taken into account explicitly in a (remap) loop over the nodes.

Uncoupling of material and nodal point displacements implies that convection has to be taken into account to update the state at the nodal points. A method to calculate this convection has been presented by Huétink.^{11, 12} The basic idea is the introduction of continuous stress and strain fields by interpolation of nodal point stresses and strains. The convective terms are calculated as a product of gradients of these continuous fields and the displacement increments. This will be elaborated for a one-dimensional example. The velocity of a material particle at a spatial location x and at time t in a one-dimensional configuration is v^m

$$v^m = dx^m/dt \quad (18)$$

with the velocity of a nodal point (v^n) a special case, obtained by replacing the superscript m by n . The material rate of change of a stress measure σ^m is

$$\dot{\sigma}^m = \left(\frac{d\sigma}{dt} \right)^m = \frac{\partial \sigma}{\partial t} + v^m \frac{\partial \sigma}{\partial x} \quad (19)$$

and the rate of change of the same stress measure in a nodal point can be obtained again by replacing the superscript m by n . Eliminating the spatial rate of the stress yields

$$\dot{\sigma}^n = \dot{\sigma}^m + (v^n - v^m) \partial \sigma / \partial x \quad (20)$$

Using a fixed mesh, i.e. a mesh in which all nodal points are fixed in space, $v^n = 0$, and the stress σ in a point with a fixed location x can be written as (Figure 1)

$$\sigma^n(x, t + \Delta t) = \sigma^n(x, t) + \dot{\sigma}^m \Delta t - (v^m \Delta t) \partial \sigma / \partial x \quad (21)$$

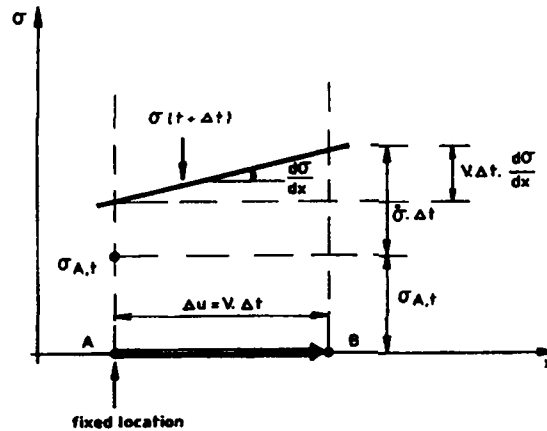


Figure 1. Update of stress state at fixed nodal point (one-dimensional example)

The third term on the right-hand side of equation (21) represents the convective stress increment. From this equation it appears that the gradient of the stress field has to be determined. The stress σ is generally not continuous at element boundaries and therefore cannot be determined directly at element level. Considering for example elements with linear interpolation of the displacement, then the strain and stress gradients vanish, which implies that convection disappears.

In the present formulation the convective contribution to the stress increment is implemented by a two-step procedure. Firstly, local least square smoothing is applied at element level, i.e. in the four noded elements used in this study a mean value of four integration points is taken. Next, average nodal point values are calculated, formally expressed by a linear map from element to nodes. By interpolation of these mean nodal point values a continuous field is obtained. This field is of course different from the internal element values. This procedure is commonly used for post-processing purposes. Initially,¹¹ the interpolated continuous field was directly used for the determination of the convective stress increment (the third term in equation (21)). However, it was observed that this formulation gave numerical instabilities depending on the size of the displacement increments.¹²

In order to avoid instabilities, equation (12) is recast in the following form:

$$\sigma(x, t + \Delta t) = \sigma(x - \Delta u^m, t) + \dot{\sigma}^m \Delta t \quad (22)$$

In fact equation (21) is a first-order spatial Taylor series expansion of equation (22). Starting from equation (22) the global smoothing procedure approximates the internal element initial values at time t . The first term in this equation (the initial stress field at time t) is replaced by the continuous stress field σ^* . This continuous stress field σ^* is based on the mapping of the nodal point values (the result of the local smoothing procedure) back to the particular locations inside the element ($x - \Delta u^m$). However, it was observed that the procedure of successive local and global smoothing results into numerical diffusion (over smoothing).¹²

Therefore in the present implementation the integration point values are not completely replaced by the values obtained by the global smoothing procedure, but are calculated as a weighed sum of equations (21) and (22). So

$$\sigma(x, t + \Delta t) = (1 - \alpha)\sigma(x, t) + \dot{\sigma}^m \Delta t - (1 - \alpha)\Delta u^m \frac{\Delta \sigma^n}{\Delta x} + \alpha[\sigma^*(x - \Delta u^m, t)] \quad (23)$$

The weight factor α for global smoothing is taken proportional to the ratio of the material displacement increment and the element size.²⁰ A reasonable range for α appears to be

$$\frac{\Delta u^m}{l_e} \leq \alpha \leq 2 \frac{\Delta u^m}{l_e} \quad (24)$$

where l_e represents the element length. In the finite element program the weight factor is automatically taken into account at element level. By introducing a weight factor which is proportional to the Courant number the smoothing is proportional to the total displacement and hence proportional to the accumulated convection.

3. EULEREAN APPROACH OF LAYERED SYSTEMS

The consequence of adding convective terms is that nodal point values as stresses and strains 'stream' through the finite element mesh or, better, a material particle moves through the mesh. However, since in the model the constitutive behaviour of the material is coupled to the fixed elements, the method is capable of giving reasonable results only for homogeneous material

throughout the complete finite element discretization. Since the geology of the subsoil generally consists of layered deposits, the model is extended in the sense that the material properties can stream through the mesh as well or, better, the material particle moves through the fixed finite element mesh including its constitutive behaviour.

3.1. Model

In order to follow the physical movement of a material particle, convection is applied to the total displacements of the nodal points. This procedure yields 'convected total displacements', analogous to the convected stresses and strains. Considering the same one-dimensional case used before, the convected total displacement of a fixed nodal point, u^n , is calculated as

$$u^n(x, t + \Delta t) = u^n(x, t) + \Delta u^m \left(1 - \frac{\partial(u^m + \Delta u^m)}{\partial x} \right) \quad (25)$$

in which the superscript n refers to a fixed nodal point, while the superscript m refers to a material related quantity. This formula differs from equation (21) in the sense that a higher-order term, the incremental displacement, is added in the derivation of the convective part. In contrast to stresses and strains the incremental displacement field is known and obeys C_0 -continuity. From equation (25) it follows that the gradient of the incremental displacement field is required to obtain the total convected displacement at a fixed nodal point. To obtain a smooth continuous field the same global smoothing procedure is applied as introduced in the derivation of the stress and strain fields.

The next step in the calculation procedure is to subtract the convected total displacements from the co-ordinates of the fixed (nodal) point P , in order to derive the original location of the material particle which now has arrived at point P :

$$\begin{aligned} x_P^O &= x_P^N - \sum_{i=1}^{nincr} \Delta u_x^P(i) \left[1 - \frac{\partial \Delta u_x^P(i)}{\partial x} \right] \\ y_P^O &= y_P^N - \sum_{i=1}^{nincr} \Delta u_y^P(i) \left[1 - \frac{\partial \Delta u_y^P(i)}{\partial y} \right] \end{aligned} \quad (26)$$

where x_P^N and y_P^N are the co-ordinates of the fixed nodal point P and $nincr$ is the total number of incremental steps. In order to get an element related quantity the average values of x_j^O and y_j^O of all nodal points connected to the element are calculated:

$$(x_{elem}^O, y_{elem}^O) = \left[\frac{\sum_{j=1}^{nnod} x_j^O}{nnod}, \frac{\sum_{j=1}^{nnod} y_j^O}{nnod} \right] \quad (27)$$

in which $nnod$ is the total number of nodes per element.

Next, it is checked whether point (x_{elem}^O, y_{elem}^O) is located inside the original domain of material A or inside the original domain of material B (Figure 2). If the material index of an element changes from A to B during an incremental step, then the boundary between the materials passes the element under consideration. The material parameters of the element are modified. The modified parameters are subsequently used both in the definition of the new tangent stiffness matrix and in the stress correction routines.

It is noted that this way of parameter adjustment may cause sudden unbalances in the numerical iteration procedure. This implies that in practice the difference between both sets of

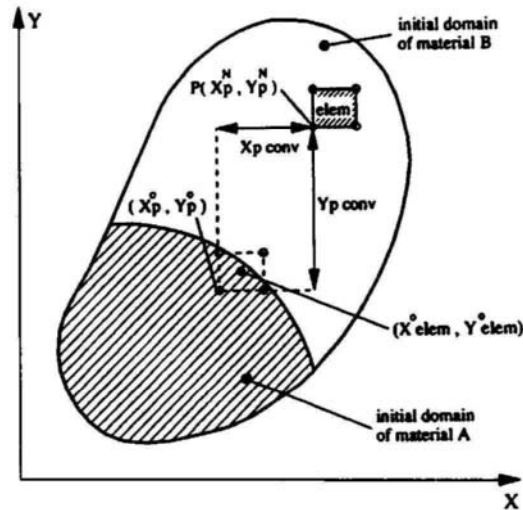


Figure 2. Definitions for moving material boundary through fixed finite element mesh

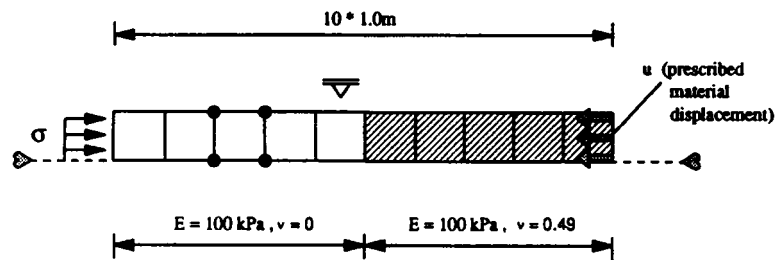


Figure 3. Finite element mesh one-dimensional example (cylinder)

material parameters is limited, depending on the element size, the stress conditions and the total number of elements.

3.2. Example

Material in a hollow cylinder is subjected to a monotonically increasing axial stress (σ), Figure 3. Simultaneously, the material moves through the cylinder in axial direction from the right-hand side to the left-hand side. Initially, the material in the right half of the cylinder differs from the material in the left part. Linear elastic material behaviour is assumed. The stiffness of both materials is identical ($E = 100 \text{ kPa}$), while Poisson's ratio ν in the right half is equal to 0.49, whereas in the other part $\nu = 0.0$. Accordingly, the stress build-up in a direction perpendicular to the axis (here called the transverse stress) is either almost equal to the axial stress ($\nu = 0.49$) or equal to zero ($\nu = 0.0$).

Two cases are considered: one without adjustment of parameters and the other one with parameter modification depending on the position of the material front. For both cases the results of four incremental steps are presented: for a material displacement $u = 0.5, 1.0, 1.5$ and 2.0 m .

Figure 4 presents the transverse stress distribution in the cylinder for the 'non-layered' calculation: although the material streams through the mesh, the material properties remain at their original position. Initially, the numerical and analytical solution are in full agreement. Due to local smoothing the transverse stress at $x = 5$ m is equal to half the value at $x = 4$ m and half the value at $x = 6$ m. At increasing material flow, however, the numerical front stays more and more behind the analytical solution. This is because the additional transverse stress build-up, caused by the axial stress increments, only takes place inside the original domain of the material with $v = 0.49$.

Figure 5 presents the result according to the 'layered' version of the Eulerian model. When the material front passes half the element width, the material properties are modified. The numerically derived transverse stress front now properly follows the theoretical solution. The difference between the theoretical and numerical distribution is caused by some numerical diffusion associated to the smoothing procedure for the determination of the convective stress increment.

4. CONSTITUTIVE MODEL

Since the two main purposes of this article are the development of an ALE algorithm for layered media and the demonstration of its applicability to soil models, and not the exact simulation of cone penetration or other *in situ* soil tests, the material model has been kept as simple as possible, incorporating only the most relevant features of inelastic soil behaviour. In this spirit a standard elastoplastic model is used with an additive decomposition of the Eulerian strain rate d_{ij} , implying that the elastic part of the deformations can be considered small with respect to the

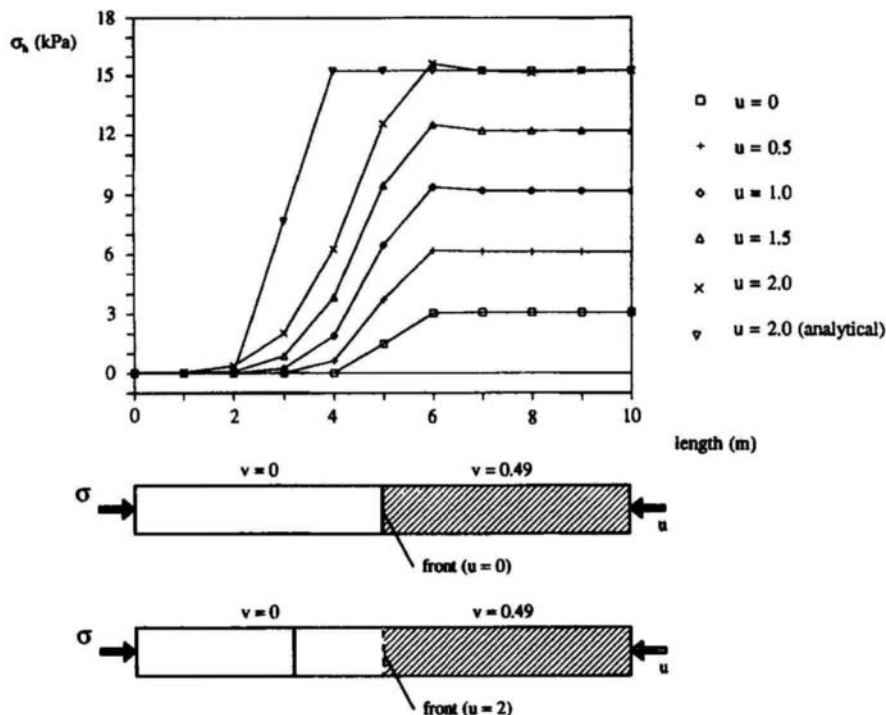


Figure 4. Transverse stress in cylinder: 'non-layered' Eulerian result and analytical solution

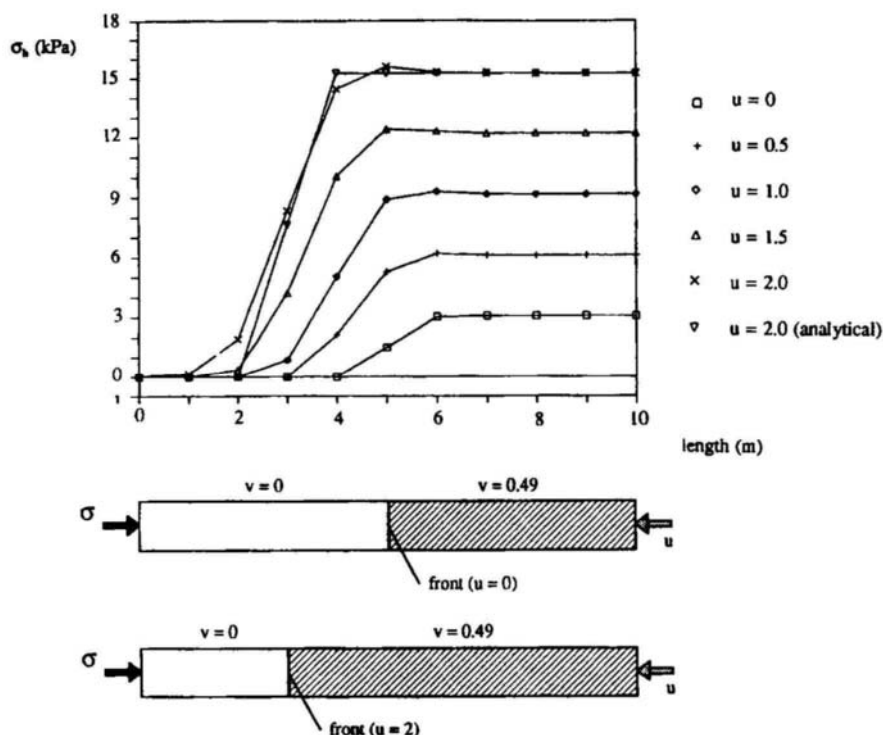


Figure 5. Transverse stress in cylinder: 'layered' Eulerian result and analytical solution

plastic part. The elastic part is related linearly to the Cauchy stress tensor via Hooke's law. Obviously, this is a gross simplification of real soil behaviour, and will quantitatively affect the outcome of the analyses that will be presented later in this article. However, qualitatively no major effects are expected to occur. A standard Drucker–Prager yield function has been adopted to bound the stresses that occur in the soil:

$$f = \sqrt{3J_2} + \alpha p - k \quad (28)$$

with J_2 the second invariant of the deviatoric stress tensor, p the hydrostatic pressure (tension considered positive), and α and k material parameters that can be related to the more familiar strength parameters c (cohesion) and ϕ (friction angle) in a standard way, e.g. by letting the outer corners of the Mohr–Coulomb yield contour coincide with the smooth Drucker–Prager approximation. It is emphasized that a good qualitative simulation of any *in situ* soil test is not attempted in this contribution, which is the reason why the assumption of a Drucker–Prager failure surface, which is a crude approximation especially for higher friction angles, is permissible.

The plasticity model is completed by a standard isotropic strain-hardening assumption and a non-associated flow rule, such that the plastic strain rate is derivable from a plastic potential function:

$$g = \sqrt{3J_2} + \beta p \quad (29)$$

with β a dilatancy factor that can be related to the more familiar dilatancy angle ψ in a fashion similar to the relation between the strength parameter α and the friction angle ϕ . As has been

discussed by many authors, starting from Reynolds,²¹ a constant dilatancy angle ψ would lead to an unrealistic volume increase, which in turn will cause an incorrect prediction of stress evolution in confined regions, for instance around the tip of a penetrating cone.

The effect discussed above can be avoided by making the dilatancy angle a function of the equivalent plastic strain $\bar{\epsilon}_{pl}$:

$$\sin \psi = \sin \psi_0 e^{\bar{\epsilon}_{pl}/\xi} \quad (30)$$

ψ_0 is the initial value of the dilatancy angle and ξ is a hardening/softening parameter which can be derived from results of large deformation triaxial tests. Considering a large number of such tests, it seems a reasonable assumption that after approximately 5 per cent shear strain, $\sin \psi$ has decreased to 50 per cent of its original value. This leads to a value $\xi = 0.072$.

We now employ Rowe's stress-dilatancy theory²² to relate the variable dilatancy angle ψ to a variable friction angle ϕ . We then obtain

$$\sin \phi = \frac{\sin \phi_{cv} + \sin \psi}{1 + \sin \psi \sin \phi_{cv}} \quad (31)$$

with $\sin \psi$ defined as in equation (30) and ϕ_{cv} the friction angle at constant volume. When we introduce definitions (30) and (31) into the Drucker-Prager model the following set of six parameters results: Young's modulus E , Poisson's ratio ν , the cohesion c , the friction angle at constant volume ϕ_{cv} , and the hardening/softening parameter ξ .

Two final aspects that merit a brief discussion are the temporal integration of the elasto-plastic rate equations and the modelling of the interface between the soil and a penetrating body. With respect to the first issue, use has been made of a one-point Euler backward integration scheme,²³ which has been shown to be unconditionally stable, to be highly accurate and to prove a rigorous satisfaction of the yield function at the end of the loading step. For the soil-structure interaction special interface elements have been used, see for instance Schellekens and De Borst,²⁴ with a Coulomb model to describe the friction mechanism:

$$\tau_{pl} = \alpha + \sigma_n \tan \delta \quad (32)$$

where τ_{pl} is the allowable shear stress level, σ_n is the normal stress at the interface, α is the adhesion and δ is the interface friction angle.

5. ANALYSIS OF CONE PENETRATION

We will now apply the procedures that have been developed to the particular case of a cone penetration test. The cone penetration test is becoming increasingly popular as an *in situ* test for site investigation and geotechnical design.⁵ A steel cylindrical bar with a diameter of 35.7 mm and a cone-shaped tip is pushed into the subsoil at a constant penetration rate of 2 cm per second. A cross-section of 10 cm² and a tip-angle of 60° is generally accepted as standard and has been specified in the European and American Standards.^{25,26} During penetration the tip reaction force is registered.

5.1. Eulerean approach of penetration process

A schematic view of an Eulerean model is presented in Figure 6. The cone is modelled as a fixed boundary and interface friction is taken into account between this boundary and the soil. The effect of the far field has been incorporated by inserted spring elements at the outer boundary of

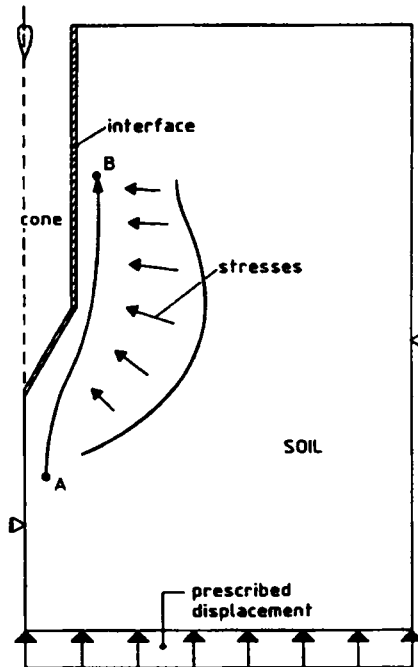


Figure 6. Schematic view of an Eulerian approach to the cone penetration problem

the finite element model. The spring stiffnesses have been determined using a cavity expansion approach. At the start of the analysis the initial state of stress is defined by the soil weight and the lateral pressure ratio at rest. So, in fact the cone is introduced into a pre-bored hole. The penetration process itself is initiated by applying incremental material displacements at the lower boundary of the mesh. Material streams upward through the mesh. As indicated in Figure 6 a material particle *A*, originally located underneath the tip of the cone, moves upward and is compressed around the shaft of the cone, arriving at, for instance, point *B*. The corresponding stress and strain fields around the cone are calculated. The calculation is stopped when a steady state is reached with respect to the stress and strain distribution in the complete finite element mesh.

5.2. Finite elements

The application of conventional eight-noded quadrilateral elements with full (nine-point) and reduced (four-point) integration do not give good results, neither for small strains,⁴ nor for large strains.⁵ A steady-state limit load could not be obtained. Even for frictionless behaviour the load-displacement curve showed a steadily increasing behaviour. These problems related to the fact that the kinematics of an elastic perfectly plastic material are highly constrained at limit loads, the so-called volumetric locking. To increase the ratio 'degrees of freedom-number of constraints', different solutions are in principle possible. The most robust strategy is probably to use higher-order displacement models, e.g. fifteen-noded triangles,^{3,4} but successful combinations of ALE techniques and higher-order displacement models seem hard to achieve. For this reason, simple four-noded elements are used, in which the constant volume condition is imposed for the average deformation of the element rather than for each of the four Gaussian points.^{27,28}

To account for the contact-frictional interface behaviour between penetrometer and soil, four-noded interface elements are incorporated in the model. To avoid stress oscillations and unrealistic stress build-up at the corner point between tip and shaft, a lumped integration scheme has been utilized.²⁴ To obtain a smooth stress state around the corner point, the shape of the cone is rounded.

5.3. Initial stresses

Since (a) deep penetration is considered (depth of cone-tip greater than, say, 10 times the cone diameter) and (b) in the model only a limited area around the cone is modelled by finite elements, the gradient of the vertical stress is of secondary importance and a homogeneous initial state of stress can be introduced into the model before starting the penetration simulation. This state of stress is characterized by $\sigma_{v,0}$, the initial vertical stress at a depth corresponding to the cone tip, and the lateral pressure ratio K_0 , defined as the ratio of the initial horizontal stress $\sigma_{h,0}$ and $\sigma_{v,0}$.

5.4. Validation of the model

A number of test runs have been performed to validate the model. In particular, the influence of the coarseness of the mesh in both perfectly plastic and softening material as well as the influence of the boundary condition at the shoulder of the cone has been analysed.

The finite element mesh used for the basic calculation consists of 360 elements and is visualized in Figure 7. The cone is assumed to be fully smooth. For this particular case, the perfectly plastic Drucker-Prager model has been applied with the following parameter values: $E = 5000$ kPa, $\nu = 0.3$, $\phi = 30^\circ$, $\psi = 0^\circ$ and $c = 2$ kPa, initial vertical stress $\sigma_{v,0} = 35$ kPa and $K_0 = 1.0$.

The calculation has been carried out using a tangential stiffness approach, updated before each iteration, and a global force unbalance criterion has been used equal to 0.1 per cent. An automatic step size correction scheme has been applied: the step size is automatically increased or decreased by a factor two, depending on the rate of convergence. After the fourth step, the maximum (prescribed) step size of 2 mm (i.e. 0.0556 times the cone diameter D) is reached. To reach a converged solution 4 to 5 iterations are needed. The complete run consists of 80 incremental steps. The load-displacement curve obtained is shown in Figure 7. After a displacement of approximately $3D$ a steady state is reached with respect to the tip reaction force.

5.5. Coarseness of the mesh

In order to study the effect of the coarseness of the finite element mesh, two additional calculations have been carried out. The basic calculation is repeated twice; once using a mesh with a quarter of the number of elements (90 instead of 360) and another using four times the element number (1440 instead of 360). The calculated load-displacement curves are also shown in Figure 7.

The difference between 90 and 360 elements is about 12 per cent whereas the difference between 360 and 1440 elements is negligible. Based on this observation the 360-element mesh will be used in the subsequent paragraphs.

5.6. Modelling the shoulder of the cone

Due to axisymmetry, the contribution of the shoulder of the cone dominates in the total reaction force. This is demonstrated by the following set of calculations, in which the boundary

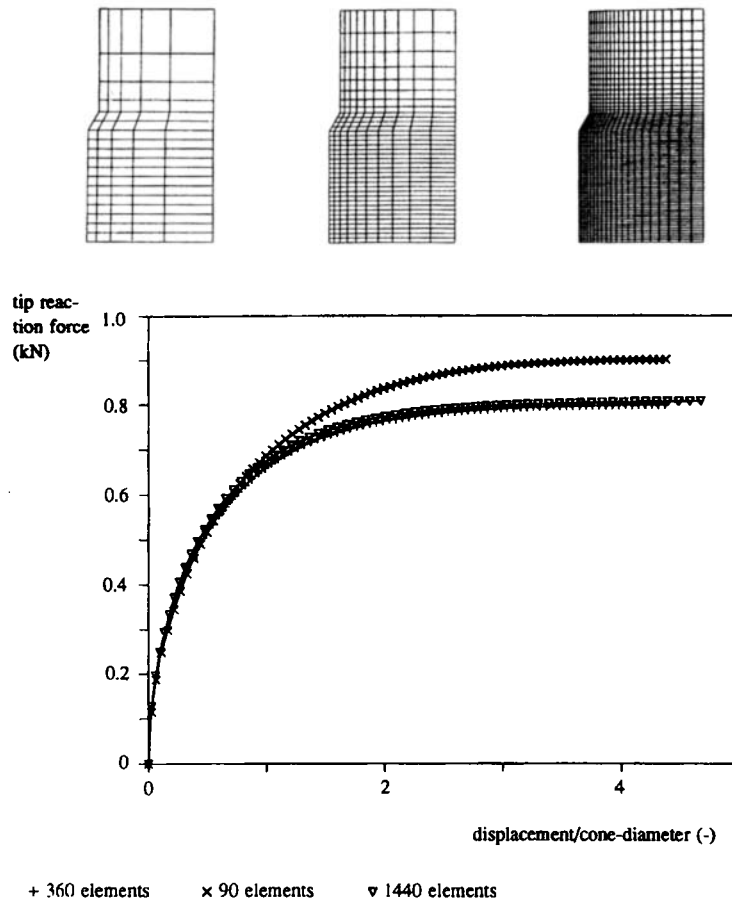


Figure 7. Load-displacement curves for 90, 360 and 1440 elements

condition at the discontinuity between the tip and the shaft is varied. Three different assumptions are shown in Figure 8. In model *A* the soil at the shoulder is forced to move in a vertical direction, whereas in model *C* the soil continues to move in a direct line with the slope of the cone tip. In model *B* the soil is forced to move in the intermediate direction.

The corresponding load-displacement curves for the finite element meshes consisting of 90 and 360 elements respectively are shown in the same figure. As can be seen, mesh refinement reduces the influence of the boundary condition. The difference between the reaction force for model *A* and for model *B* can be interpreted as the result of a sort of 'reduced fictitious cone diameter'. Model *A* can be regarded as a cone with a radius equal to the radius according to model *B* minus half the element width at the left-hand side of the shoulder point. Following the same line of reasoning, in model *C* the fictitious radius can be interpreted to be enlarged by half the element width at the right-hand side of this point.

5.7. Strain softening and mesh objectivity

Classical continuum models, i.e. models that do not incorporate an internal length scale, suffer from mesh-dependence when strain-softening models are employed in numerical analyses. When

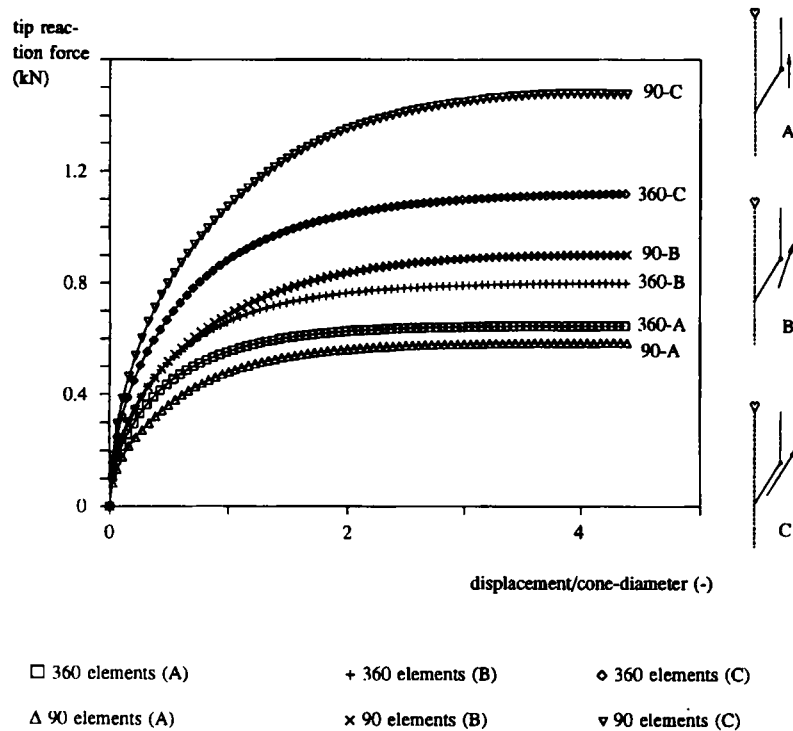


Figure 8. Influence boundary condition at the shoulder of the cone

a strain localization zone develops, the governing differential equations lose ellipticity. To regularize the equations after localization, there are at least four different approaches: (1) Cosserat theory,²⁹ (2) non-local plasticity theory,³⁰ (3) gradient plasticity theory³¹ and (4) rate-dependent models, each of them having its own advantages and disadvantages.³²

In order to quantify the effect of mesh dependence for the specific case of cone penetration in softening material, four calculations have been performed using the 90 and 360 element meshes. In two runs the material behaviour is assumed to be perfectly plastic, whereas in the other runs the softening model is used. The initial vertical stress is 35 kPa and K_0 is equal to 1.0. The results are shown in Figure 9.

It can be seen that the difference between the two perfectly plastic curves is about the same as the difference between the two softening curves. The ratio 'limit load for 360 elements over limit load for 90 elements' is 0.83 for the perfectly plastic model and 0.85 for the softening model. Based on this observation, it is assumed that for the cone penetration problem there is not so much mesh sensitivity, at least within the range of parameters occurring in geotechnical practice. The reason is that most of the material softening takes place during the phase in which the total reaction force working on the cone still increases and in which localization does not yet occur.

6. PENETRATION IN LAYERED SOIL

The subsoil consists of layered deposits with different thicknesses and properties. During the interpretation of measured data one has to consider the effects of a cone passing through the

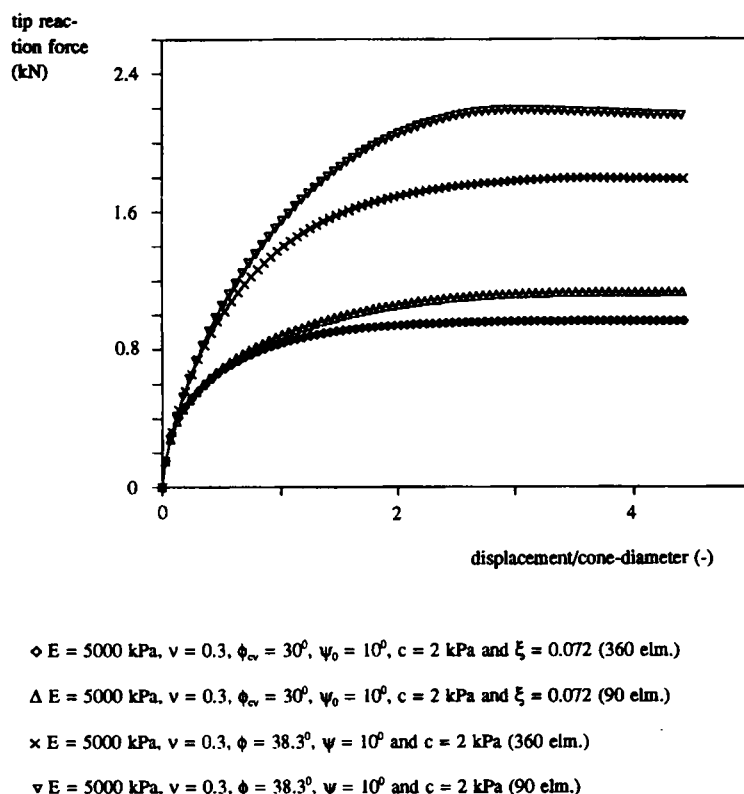


Figure 9. Load-displacement curves for perfectly plastic and strain softening material (90 and 360 elements)

boundaries between soil layers. So far, the answers to those questions have been highly empirical and are based on a relatively small number of experiments.³³ Calibration chamber tests for sand^{34,35} show that the cone tip senses an interface between 5 and 10 cone diameters ahead and behind. They also indicate that the distance over which the cone resistance is influenced increases with increasing soil stiffness difference. This implies that for interbedded sand deposits the minimum stiff layer thickness to ensure full tip resistance is equal to 10–20 times the cone diameter, i.e. 36 to 72 cm. For undrained clay layers, however, the minimum thickness of a layer to generate the full cone resistance, is considerably lower: 2 to 4 times the cone diameters or 7 to 15 cm.³⁴

In this section two systems are studied numerically, referred to as 'clay on sand' and 'sand on clay'. It is emphasized that the studies are of a qualitative nature. For obtaining more precise data that are directly relevant to geotechnical practice more refined constitutive models and much more parameter studies must be undertaken. The initial state of stress, for the sample calculations together with the material parameters are given in Table I.

6.1. Clay on sand

The first simulation is related to cone penetration from a (soft) clay layer into a (stiffer) sand layer. At the beginning of the analysis the clay-sand boundary is located at 46.2 mm below the tip of the cone (see Figure 10). The calculated load-displacement curve is presented in Figure 11,

Table I. Material parameters and initial stresses adopted in the calculations

	Clay	Sand
E (kN/m ²)	2000	5000
ν	0.49	0.3
c (kN/m ²)	10	2
ϕ_{cv} (°)	—	30
ψ_0 (°)	—	10
ξ	—	0.072
σ_{v0} (kN/m ²)	35	35
K_0	1.0	1.0
δ (°)	—	10
a (kN/m ²)	6.67	0.667

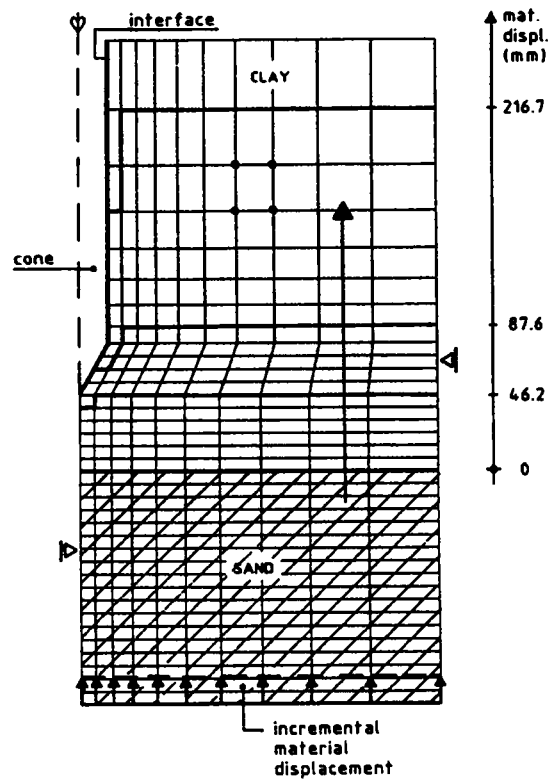


Figure 10. Finite element mesh and location of clay-sand boundary during penetration

which also gives the curves for homogeneous clay and homogeneous sand. The discontinuities of the two-layer line are related to the fact that at that specific points, modification of material properties from clay to sand takes place in the soil and/or in interface elements located close to the tip of the cone.

From Figure 11, it can be concluded that for this particular case, 15 cm penetration into the sand layer is needed to reach a new steady-state cone resistance. This is about four times the cone

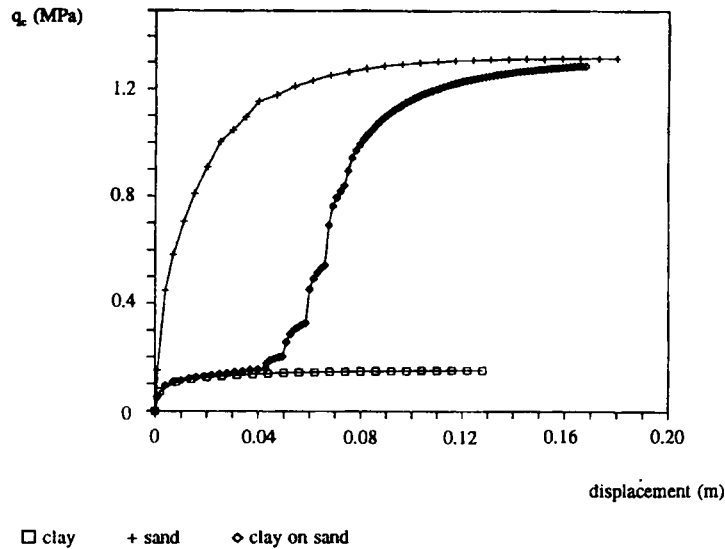


Figure 11. Load-displacement curves for homogeneous sand, homogeneous clay and 'clay on sand'

diameter. Figure 10 presents the position of the boundary between the layers at four different stages during penetration. It can be seen that the boundary between both layers does not remain horizontal. In front of the cone tip hardly any influence can be noticed. However, when the boundary moves upward along the tip of the cone towards the shoulder some clay sticks to the cone and a thin clay film remains between the shaft and the sand layer, even when the boundary is at a position of several diameters above the cone tip.

In order to investigate the influence of the stiffness ratio between sand and clay layer, two additional calculations have been carried out: (a) the stiffness of the sand is decreased to the stiffness of the clay ($E_{\text{sand}} = 2000 \text{ kPa}$) and (b) the stiffness is increased to $E_{\text{sand}} = 8000 \text{ kPa}$. The calculated load-displacement curves are shown in Figure 12. It is clear that the slope of the curve strongly depends on the stiffness ratio. The gradient of the cone resistance per unit depth increases with increasing stiffness. For $E_{\text{sand}} = E_{\text{clay}} = 2000 \text{ kPa}$, the gradient of the cone resistance is equal to about $0.095 \text{ MPa per cm penetration}$, while this value increases to 0.172 for $E_{\text{sand}} = 5000 \text{ kPa}$, and to 0.213 MPa/cm for $E_{\text{sand}} = 8000 \text{ kPa}$. Since the stiffness of sand is generally large when compared to the stiffness of clay, the gradient of the cone resistance measured at the clay-sand boundary is dominated by the sand layer and thus provides information about the sand stiffness.

The penetrating distance into the sand layer necessary to arrive at the new steady-state value increases with increasing stiffness. For $E_{\text{sand}} = E_{\text{clay}}$ the interval during which the cone resistance rises to the new level is limited to the vertical length of the cone tip. If the cone tip is fully embedded in the sand layer, a steady state is reached immediately. For $E_{\text{sand}} = 2.5 \times E_{\text{clay}}$, the distance necessary to reach the full resistance is approximately equal to $3D$, while this length increases to $5D$ for $E_{\text{sand}} = 4 \times E_{\text{clay}}$.

6.2. Sand on clay

The second system concerns penetration from a sand layer into a clay layer. At the start of the simulation the boundary between sand and clay is located between the first and the second

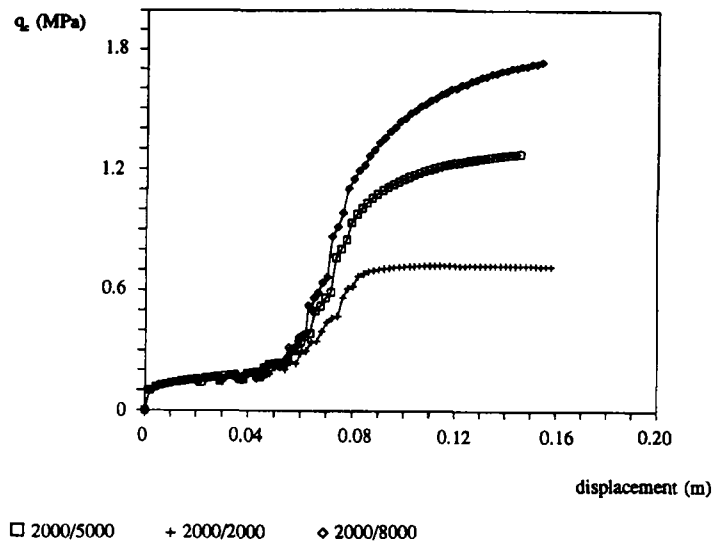


Figure 12. Load-displacement curves for different stiffness-ratios between clay and sand layer ($E_{\text{clay}}/E_{\text{sand}}$)

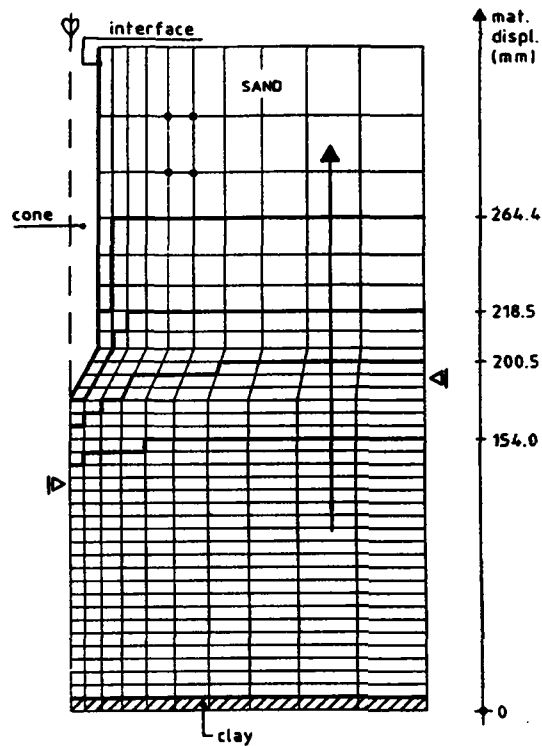


Figure 13. Finite element mesh and location of sand-clay boundary during penetration

element at the lower side of the mesh, i.e. 177.1 mm under the tip of the cone (Figure 13). The load–displacement curve calculated is presented in Figure 14. For this particular case, the cone resistance starts to drop at a distance of about 10 cm above the clay boundary. The cone senses the soft layer at a distance of about $3D$.

In order to investigate the influence of stiffness, the stiffness ratio between the (stiffer) sand layer and the (soft) clay layer is varied. Two additional calculations have been carried out: (a) the

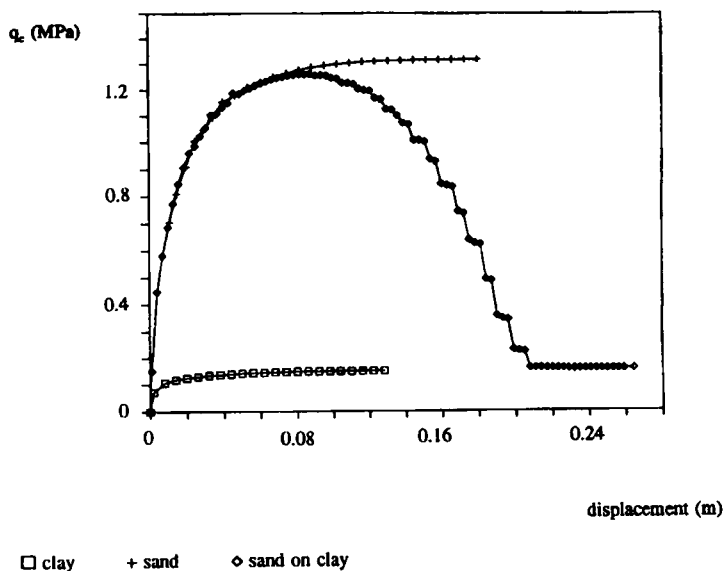


Figure 14. Load–displacement curves for homogeneous sand, homogeneous clay and 'sand on clay'

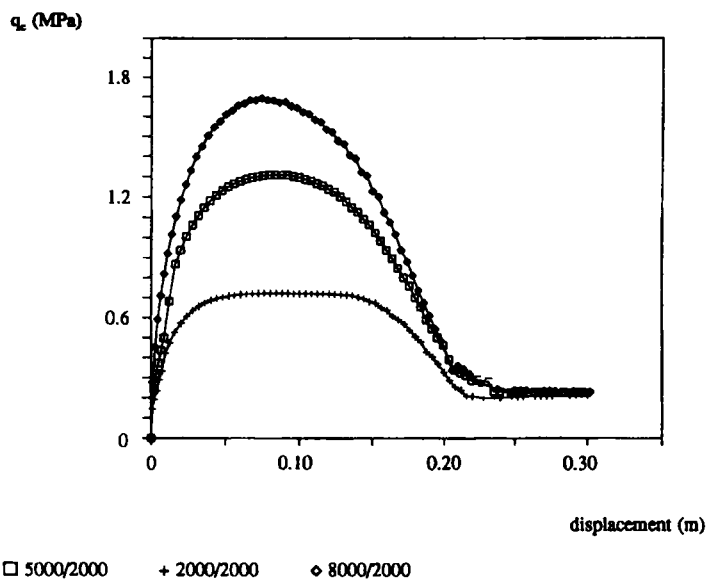


Figure 15. Load–displacement curves for different stiffness-ratios between clay and sand layer (E_{sand}/E_{clay})

stiffness of the sand is decreased to the stiffness of the clay layer ($E_{\text{sand}} = E_{\text{clay}}$) and (b) the stiffness is increased to $E_{\text{sand}} = 4 \times E_{\text{clay}}$. The corresponding load–displacement curves are shown in Figure 15. Obviously the shape of the curve strongly depends on the stiffness ratio. The steepness of the curve increases with increasing sand stiffness. If the stiffnesses are equal, the cone senses the next layer when the tip reaches it. For this particular case the new steady-state cone resistance is reached immediately after the tip of the cone is fully embedded in the clay. For $E_{\text{sand}} = 2.5 \times E_{\text{clay}}$ the cone senses the soft layer at a distance of $3D$ and for $E_{\text{sand}} = 4 \times E_{\text{clay}}$ at a distance of about $4D$. As can be seen in Figure 13 at some distance ahead the relatively stiff sand is pushed into the soft clay layer. At continued penetration some sand remains between the shaft of the cone and the clay, smeared out over a length of about 50 mm.

7. CONCLUSIONS

An Eulerian finite element model has been presented, which is a special case of a more general Arbitrary Lagrangean Eulerian (ALE) approach. In contrast to an Updated Lagrangean approach, in which large element distortion can cause numerical problems, the penetrating length is no longer a limitation.³⁶ A minor drawback of the Eulerian approach is related to the fact that due to smoothing inherent to the convection algorithm some numerical diffusion is introduced. On the other hand, the smoothing technique increases the stability of the calculation procedure.

The model has been applied to simulate cone penetration in layered soil. The strength of the sand is characterized by a non-associative Drucker–Prager criterion depending on peak and critical friction angles and the undrained clay behaviour is modelled using a Von Mises criterion. The results suggest that a cone coming out of a sand layer senses a soft clay layer at a distance of about three times the diameter of the cone. Simulation of cone penetration from soft clay into sand shows that a penetrating distance of at least four times the diameter is needed into the sand layer to reach the new steady-state cone resistance corresponding to that layer. However, these results are strongly dependent on the material properties of the layers. Especially the stiffness ratio between the layers plays an important role.

ACKNOWLEDGEMENTS

The results presented form part of a study commissioned by the Construction Division and the Road and Hydraulic Division of the Dutch Ministry of Public Works. The commission of that contract is gratefully acknowledged.

REFERENCES

1. A. S. Vesic, 'Expansion of cavities in infinite soil mass', *Int. J. Soil Mech. Found. Div. ASCE*, **98**, 265–290 (1972).
2. M. M. Baligh, *The Strain Path Method*, Lecture I, MIT Special Summer Course, MIT, Cambridge, MA 02139, 1985.
3. R. de Borst and P. A. Vermeer, 'Possibilities and limitations of finite elements for limit analysis', *Geotechnique*, **34**(2), 199–210 (1984).
4. R. de Borst, 'Calculation of collapse loads using higher order elements', in P. A. Vermeer and H. J. Luger (eds), *Proc. IUTAM Symp. Deformation and Failure of Granular Materials*, 1982, pp. 503–513.
5. P. van den Berg and P. A. Vermeer, 'Undrained strength from CPT and finite element computations', *Proc. 6th Int. Conf. on Numer. Methods in Geom.*, Innsbruck, 1988, pp. 1095–1100.
6. P. D. Kioussis, G. Z. Voyiadjis and M. T. Tumay, 'A large strain theory and its application in the analysis of the cone penetration mechanism', *Int. j. numer. anal. methods in geomech.*, **12**, 45–60 (1988).
7. A. Cividini and G. Gioda, 'A simplified analysis of pile penetration', *Proc. 6th Int. Conf. on Numer. Methods in Geom.*, Innsbruck, 1988, pp. 1043–1049.

8. T. J. R. Hughes, W. K. Liu and T. K. Zimmermann, 'Lagrangean-Eulerian finite element formulation for incompressible viscous flow', *Comput. methods appl. mech. eng.*, **29**, 329-349 (1981).
9. J. Donea, 'Arbitrary Lagrangean-Eulerian finite element method. Comp. Meth. for transient analysis', in T. Belytschko and T. J. R. Hughes (eds), *Comp. methods mech.*, Vol. 1, North-Holland, Amsterdam, 1983.
10. W. K. Liu, T. Belytschko and H. Chang, 'An arbitrary Lagrangean-Eulerian finite element method for path dependent materials', *Comput. methods appl. mech. eng.*, **58**, 227-245 (1986).
11. J. Huétink, 'Analysis of metal forming processes based on a combined Eulerian-Lagrangean finite element formulation', in Pittman et al. (eds), *Proc. Int. Conf. Num. Meth. Industr. Forming Processes*, Pineridge Press, Swansea, 1982, pp. 501-509.
12. J. Huétink, 'On the simulation of thermomechanical forming processes', *Ph.D. Thesis*, University of Enschede, The Netherlands, 1986.
13. J. F. Besseling, 'Models of metal plasticity; theory and experiment', in A. Sawczuk and G. Bianchi (eds), *Plasticity Today*, Elsevier, Amsterdam, 1985, pp. 97-113.
14. G. C. Johnson and D. J. Bammann, 'A discussion of stress rates in finite deformation problems', *Int. j. solids struct.*, **20**, 725-737 (1984).
15. L. Szabo and M. Balla, 'Comparison of some stress rates', *Int. j. solids struct.*, **25**(3), 279-297 (1989).
16. Y. M. Cheng and Y. Tsui, 'Limitations to the large strain theory', *Int. j. numer. methods eng.*, **33**, 101-114 (1992).
17. D. F. E. Stolle and H. Schad, 'An updated reference configuration formulation for large-strain problems', *Int. j. numer. anal. methods geomech.*, **16**, 295-306 (1992).
18. R. M. McMeeking and J. C. Rice, 'Finite element formulation for problems of large elastoplastic deformation', *Int. J. Solids Struct.*, **11**, 611-616 (1975).
19. K. J. Bathe, E. Ramm and E. L. Wilson, 'Finite element formulations for large deformation dynamic analysis', *Int. j. numer. methods eng.*, **9**, 353-386 (1975).
20. J. Huétink and P. van der Helm, 'On Euler-Lagrange finite element formulation in forming and fluid problems', in Chenot et al. (eds), *Proc. Int. Conf. Numer. Methods Industr. Forming Processes*, Balkema, Rotterdam, 1992, pp. 45-54.
21. O. Reynolds, 'On the dilatancy of media composed of rigid particles in contact', *Phil. Mag. 5th Series*, **20**, (1885).
22. P. W. Rowe, 'The stress-dilatancy relation for static equilibrium of an assembly of particles in contact', *Proc. Roy. Soc.*, **269**, 500-527 (1962).
23. R. de Borst, 'Integration of plasticity equations for singular yield functions', *Comput. struct.*, **26**(5), 823-829 (1987).
24. J. C. J. Schellekens and R. de Borst, 'On the integration of interface elements', *Int. j. numer. methods eng.*, **30**, 43-66 (1992).
25. ISSMFE, 'Report of subcommittee on standardization of penetration testing in Europe', *Proc. 9th ISSMFE Conf.*, Tokyo, Vol. 3, 1977, pp. 95-152.
26. ASTM Designation D3443, *Standard Method for Deep Quasi-static Cone and Friction-cone Penetration Tests in Soil*, 1979.
27. J. C. Nagtegaal, D. M. Parks and J. C. Rice, 'On numerical accurate finite element solutions in the fully plastic range', *Comput. methods appl. mech. eng.*, **4**, 153-177 (1974).
28. T. J. R. Hughes, *The Finite Element Method, Linear Static and Dynamic Finite Element Analysis*, Prentice-Hall, Englewood Cliffs, N.J. 1987.
29. R. de Borst, 'Simulation of strain localisation: A reappraisal of the Cosserat continuum', *Eng. Comput.*, **8**, 317-332 (1991).
30. Z. P. Bazant and F.-B. Liu, 'Nonlocal yield limit degradation', *Int. j. numer. methods eng.*, **26**, 1805-1823 (1988).
31. R. de Borst and H. -B. Mühlhaus, 'Gradient-dependent plasticity: formulation and algorithmic aspects', *Int. j. numer. methods in Eng.*, **35**, 521-539 (1992).
32. L. J. Sluys, 'Wave Propagation, Localization and Dispersion in Softening Solids', *Ph.D. Thesis*, Delft University of Technology, 1992.
33. P. K. Robertson and R. G. Campanella, *Guidelines for Use and Interpretation of the Electric Cone Penetration Test*, Hogentogler & Company Manual, 3rd edn (1986).
34. D. D. Treadwell, 'The influence of gravity, prestress, compressibility and layering on soil resistance to static penetration', *Ph.D. Thesis*, Berkeley, 1975.
35. J. H. Schmertmann, Guidelines for cone penetration test, performance and design, *Federal Highway Adm. Report FHWA-TS-78-209*, Washington, 1978.
36. P. van den Berg, 'Analysis of soil penetration', *Ph.D. Thesis*, Delft University of Technology, ISBN 90-407-1004-X, 1994.